

Quasi in-situ analysis of geometrically necessary dislocation density in α -fibre and γ -fibre during static recrystallization in cold-rolled low-carbon Ti-V bearing microalloyed steel

Kapoor, I., Lan, Y., Rijkenberg, A., Li, Z. & Janik, V. Author post-print (accepted) deposited by Coventry University's Repository

Original citation & hyperlink:

Kapoor, I, Lan, Y, Rijkenberg, A, Li, Z & Janik, V 2018, 'Quasi in-situ analysis of geometrically necessary dislocation density in α -fibre and γ -fibre during static recrystallization in cold-rolled low-carbon Ti-V bearing microalloyed steel' *Materials Characterization*, vol. 145, pp. 686-696.

<https://dx.doi.org/10.1016/j.matchar.2018.09.032>

DOI 10.1016/j.matchar.2018.09.032

ISSN 1044-5803

Publisher: Elsevier

NOTICE: this is the author's version of a work that was accepted for publication in *Materials Characterization*. Changes resulting from the publishing process, such as peer review, editing, corrections, structural formatting, and other quality control mechanisms may not be reflected in this document. Changes may have been made to this work since it was submitted for publication. A definitive version was subsequently published in *Materials Characterization*, Vol 145, 2018. DOI: 10.1016/j.matchar.2018.09.032

© 2017, Elsevier. Licensed under the Creative Commons Attribution-NonCommercial-NoDerivatives 4.0 International

<http://creativecommons.org/licenses/by-nc-nd/4.0/>

Copyright © and Moral Rights are retained by the author(s) and/ or other copyright owners. A copy can be downloaded for personal non-commercial research or study, without prior permission or charge. This item cannot be reproduced or quoted extensively from without first obtaining permission in writing from the copyright holder(s). The content must not be changed in any way or sold commercially in any format or medium without the formal permission of the copyright holders.

This document is the author's post-print version, incorporating any revisions agreed during the peer-review process. Some differences between the published version and this version may remain and you are advised to consult the published version if you wish to cite from it.

Quasi in-situ analysis of geometrically necessary dislocation density in α -fibre and γ -fibre during static recrystallization in cold-rolled low-carbon Ti-V bearing microalloyed steel

Ishwar Kapoor^{a,*}, Yongjun Lan^b, Arjan Rijkenberg^c, Zushu Li^a and Vit Janik^{a, d}

^a WMG, University of Warwick, Coventry, CV4 7AL, UK;

^b Tata Steel, Coventry Technology Centre, Coventry, CV4 7EZ, UK;

^c Tata Steel, 1970 CA IJmuiden, The Netherlands;

^d Institute for Future Transport and Cities, Coventry University, Coventry, CV1 5FB, UK

*Corresponding author at: WMG, University of Warwick, Coventry, CV4 7AL, UK

E-mail addresses: I.Kapoor@warwick.ac.uk (I.Kapoor), yongjun.lan@tatasteelurope.com (Y.Lan), arjan.rijkenberg@tatasteelurope.com (A. Rijkenberg), z.li.19@warwick.ac.uk (Z.Li) and V.Janik@warwick.ac.uk (V.Janik)

Abstract

In the present study, cold-rolled low-carbon steel is annealed at three different conditions: 700 °C for 0 s, 800 °C for 0 s and 800 °C for 2 min at the heating rate of ~10 °C/s. Recrystallization behaviour on sample surface is studied using a heated stage Scanning Electron Microscopy and Electron Backscattered Diffraction. For the lower annealing temperature of 700 °C with no dwell, almost no recrystallization is observed and microstructure resembles the as-received deformed material with the exception of occasional sub-micron sized nuclei. For the annealing conditions of 800 °C 0 s and 800 °C 2 min, onset and evolution of recrystallization is observed *in-situ* as a function of the initial as-cold rolled texture. Slower recovery rate of alpha fibre than gamma fibre is observed and confirmed by lower drop in average geometrically necessary dislocation (GND) density for un-recrystallized alpha fibres (1.1E+14 m⁻² for 700 °C 0 s, 1.4E+14 m⁻² for 800 °C 0 s and 4.5E+14 m⁻² for 800 °C 2 min) than for un-recrystallized gamma fibre grains (3.0E+14 m⁻² for 700 °C 0 s, 6.2E+14 m⁻² for 800 °C 0 s and 9.8E+14 m⁻² for 800 °C 2 min) during annealing. Strong gamma texture in recrystallized matrix is found for annealing conditions of 800 °C 0 s and 800 °C 2 min. From TEM characterisation it was shown that sub-grain boundaries are decorated with fine precipitates (diameter $d < 15$ nm) of titanium-vanadium carbides (Ti,V)C for the annealing condition of 700 °C 0 s, which suggests that these precipitates play a major overall role in retardation of the recrystallization kinetics.

Keywords: annealing; recovery; recrystallization; grain growth; geometrically necessary dislocations

1. Introduction

The extent of recrystallization in metallic engineering materials including steels and Al-, Mg-, and Ti-alloys is dependent upon chemical composition and annealing conditions such as temperature and dwell

time [1,2]. Complete control of the kinetics of recrystallization and of the recrystallized texture during the production of steel is desired to balance strength and ductility, the two parameters critical in areas such as automotive light-weighting [3–6]. In interstitial-free high-strength steels (IFHS) the development of a strong $\{111\}$ fibre parallel to the normal direction (so called gamma fibre) is favourable during annealing since it leads to an increase in deep drawing ability which enhances manufacturing capability and design freedom [7]. In low carbon steels, fine recrystallized grains [8] with a strong gamma texture are also considered beneficial [3,9]. However, because of the non-homogeneity of the thermal and strain distribution during industrial-scale steel manufacturing and due to different responses of the polycrystalline material to the external load, various textural components with different stored energies emerge, causing heterogeneous recrystallization, variation in final grain size, and deviations from the ideal optimal texture [10,11].

With the advancement of hot stage Electron Back-Scattered Diffraction (EBSD) it is possible to study instantaneously the microstructural changes during annealing [12–20]. Kerisit et al. studied microstructural evolution in Ta-alloy to evaluate nucleation rate, grain growth rate and grain boundary velocity by generating EBSD scans at certain time intervals during in-situ annealing [21]. By comparing the EBSD IPF maps taken from the same sample location and at the same magnification before and after the annealing, so called *quasi in-situ* EBSD [22] allows us to understand the role of particular microstructural components upon the kinetics of the ongoing microstructural changes. The role of twins [23] or shear bands [22] on the development of recrystallized texture during annealing has been recently studied in Mg-alloy WE43. The role of strain-induced boundary migration (SIBM) on the amount of recrystallization for Al-alloy deformed at low (strain, $e < 0.7$) and high (strain, $e > 1.4$) strains have been previously analysed using in-situ EBSD [24]. Therefore, from hot stage *quasi in-situ* EBSD investigation, it is possible to locate nucleation sites and understand further development of fully recrystallized grains which is not feasible in case of ex-situ post-mortem EBSD analysis on the microstructure of muffle furnace annealed bulk samples [12].

During cold rolling of low-carbon hot-rolled steels, two main texture families are formed: $\langle 110 \rangle$ parallel to rolling direction (alpha fibre), and $\langle 111 \rangle$ parallel to normal direction (gamma fibre) [3,9]. For cold rolled steel, stored energy is different for different grain orientations. Dillamore et al. [25] reported stored energy in alpha fibre is in the order of $SE_{\{100\}\langle 011 \rangle} < SE_{\{112\}\langle 011 \rangle} < SE_{\{111\}\langle 011 \rangle}$ based on the subgrain misorientation measurements. With an increase in rolling reduction, the intensity of both fibres is enhanced [26,27]. Wauthier-Monnin et al. carried out dislocation density analyses for alpha and gamma fibres for different rolling strains (between 15 % and 93 %). Their study revealed a dislocation density $7.25E+15 \text{ m}^{-2}$ of the $\{111\}\langle 112 \rangle$ grain orientation in the gamma fibre as compared to $4.28E+15 \text{ m}^{-2}$ of the $\{100\}\langle 110 \rangle$ and $1.35E+15 \text{ m}^{-2}$ of the $\{112\}\langle 110 \rangle$ grain orientations in the alpha fibre. Due to an increment in the intragranular misorientation in the grain orientation $\{111\}\langle 112 \rangle$ of the gamma fibre at ~76% rolling strain, there is a significant increase in the dislocation density [26].

Since stored energy (SE) is linearly dependent on the dislocation density, the difference in the stored energy of the alpha and gamma fibres is reflected in the difference in the recrystallization rate of both fibres during annealing [7,14,28–30].

Dislocations are comprised of geometrically necessary dislocations (GND) and statistically stored dislocation (SSD); GNDs are dislocations with the same signs which are formed in the strain gradient region and satisfy the geometrical constraints with a net non-zero Burgers vector, whereas SSDs constitutes random dislocations formed by mutual trapping process with a net zero Burgers vector during plastic deformation [26,31–34]. According to Ashby's model for homogenous deformation of a single crystal, SSD have dominant role in work hardening. While in the case of non-homogenous deformation of polycrystalline materials, both SSD and GND are generated but the rate of GND generation is high which makes the density of GND higher than the density of SSD and thus has a significant role in work hardening phenomena [31,34]. Calculation of SSD density is possible using Transmission Electron Microscopy (TEM), but it is a time consuming process with limited statistical significance and reduced accuracy due to artefacts created during TEM sample preparation [26,34–36]. One the other hand, from the local average misorientation map obtained from EBSD data, GND density can easily be evaluated [35] using the relation given by Kubin and Mortensen [37] relating misorientation angle ' Θ ' and GND density based on strain gradient model as proposed by Gao et al. [38].

Apart from different fibres with different stored energies, the recrystallization kinetics is also affected by the presence of precipitates, their size, volume fraction and distribution within the ferrite matrix. Fine precipitates ($d < 15$ nm) are effective in pinning grain boundaries by Zener pinning force [39,40]. Precipitates in the ferrite matrix can be present inside grains or on microstructural defects such as dislocations and sub-grain boundaries [29,41]. Therefore, recrystallization texture is also dependent on the precipitate distribution in microstructural regions corresponding with alpha or gamma fibres: if precipitates actively pins grain boundaries (GBs) of gamma fibres then during annealing it gives advantage to other grain orientations to preferably recrystallize, which results in weak gamma texture [28]. Wang et al. studied the effect of Nb atoms and Nb precipitates on the kinetics of austenite-ferrite (A-F) phase transformation in low-carbon steel. From TEM analysis, it was reported that ferrite growth is retarded by interfacial segregation of Nb solute atoms more than by the precipitates pinning on the interface via Nb precipitates [42]. Clark et al. performed FIB-lift out TEM analysis on the interphase of A-F during phase transformation from austenite to ferrite to investigate VC/VN interphase precipitate distribution and reported that the precipitates were distributed in irregularly spaced curvilinear patterns [15]. It has been demonstrated that FIB lift-out TEM analysis allows to investigate site specific chemical distribution of the solute atoms or precipitates, and to monitor their interaction with the grain boundary [15,42,43].

This paper aims to apply correlative and *quasi* in-situ material characterisation techniques to investigate recrystallization behaviour and evolution of alpha and gamma fibres by analysing geometrically necessary dislocation (GND) density in respective fibres during annealing of cold-rolled steel microalloyed with Titanium (Ti) and Vanadium (V). FIB-lift out TEM is utilised to investigate specifically precipitate size and distribution along subgrain and grain boundaries and inside recrystallized grains. Three hypotheses are explored in this paper:

- Recrystallization kinetics is higher in the gamma fibre as compared to the alpha fibre during annealing due to higher initial stored energy during deformation.
- After annealing, drop in the GND density is more significant in case of gamma fibre as compared to the alpha texture because of higher initial driving force for nucleation of recrystallization.
- During annealing at 700 °C and 800 °C the precipitates are fine, decorating sub-grain and grain boundaries and delaying further kinetics of recrystallization; with increase in dwell time to 2 min at 800 °C, precipitate size is increased and precipitates are found inside the recrystallized grains.

2. Experiment Procedures

2.1. Hot Stage *quasi* in-situ EBSD of cold rolled microalloyed steel

Cold rolled low carbon steel microalloyed with vanadium and titanium containing 0.05 C, 0.008 Si, 0.34 Mn, 0.001 P, 0.0007 S, 0.032 Al, 0.15 V, 0.078 Ti, 0.0022 N and rest Fe (all wt. %) was provided by Tata Steel Europe. During cold rolling sheet material was deformed to a 70% reduction, leading to a final sheet thickness of 1 mm. Samples for hot-stage *quasi* in-situ EBSD were cut parallel to the Rolling Direction (RD) - Normal Direction (ND) plane from the central part of the rolled sheet, machined to the size of 6 x 1 x 1 mm (Fig. 1) and mounted in Bakelite. Samples were polished using standard metallographic techniques. After polishing, the samples were extracted from Bakelite and placed onto a Gatan Murano 525 heating stage [44] with the Rolling Direction (RD) parallel to X-axis, Transverse direction (TD) parallel to Z-axis and Normal direction (ND) parallel to Y axis of the sample holder coordinate axis system inside of the chamber of a FEG-SEM Carl Zeiss Gemini fitted with NordlysNano EBSD camera by Oxford Instruments [45]. Samples were annealed at three different conditions: 700 °C for 0 s, and 800 °C for 0 s and 800 °C for 2 min at the heating rate of ~10 °C/s and then cooled down to ambient temperature inside the SEM chamber.

For the EBSD data acquisition, an accelerating voltage of 20 kV, an aperture size of 240 µm with working distance of 22 mm and a step size of 0.15 µm were used. Site specific EBSD scans at magnification of x5k of the same locations of the material were taken prior and after heating the sample. Upon cooling, the sample temperature was stabilised at 200 °C to maintain thermal equilibrium and to

minimise the thermal drift [14]. For post processing of the EBSD results, files were exported into HKL Channel 5 software of Oxford Instruments. Normal direction Inverse Pole Figure (ND-IPF) maps were obtained from channel 5 software representing the crystal orientation alignment with respect to the normal direction, ND of the sample. Local average misorientation (LAM) maps with kernel size of 7×7 ($n=3$) were used to quantify fraction of recrystallized grains and GND density by exporting .ctf files to MTEX texture analysis toolbox, MTEX-4.5.0 available in MATLAB R2016b (<http://mte-toolbox.github.io/>) [46]. Average GND density is calculated from local average misorientation to further evaluate stored energy (contribution from GND density only) on the same methodology as mentioned by Wauthier-Monnin et al., Betanda et al. and Huang et al. [26,32,47] to understand the difference in rate of recrystallization of respective fibres during annealing at different conditions [7,14,28–30]. To evaluate a noise free GND density, the LAM value of all points were calculated and plotted based on a kernel size of 11×11 ($n=5$) to 3×3 ($n=1$) as described by Moussa et al. [48]. The LAM value for 0^{th} neighbour ($n=0$) was evaluated after extrapolation and used as an average measurement for the noise. For a deformed matrix, the average measurement noise is about 0.71° whereas for a recrystallized matrix this is about 0.25° [48,49]. The average measurement for the noise were used to eliminate noise from the average GND values [48].

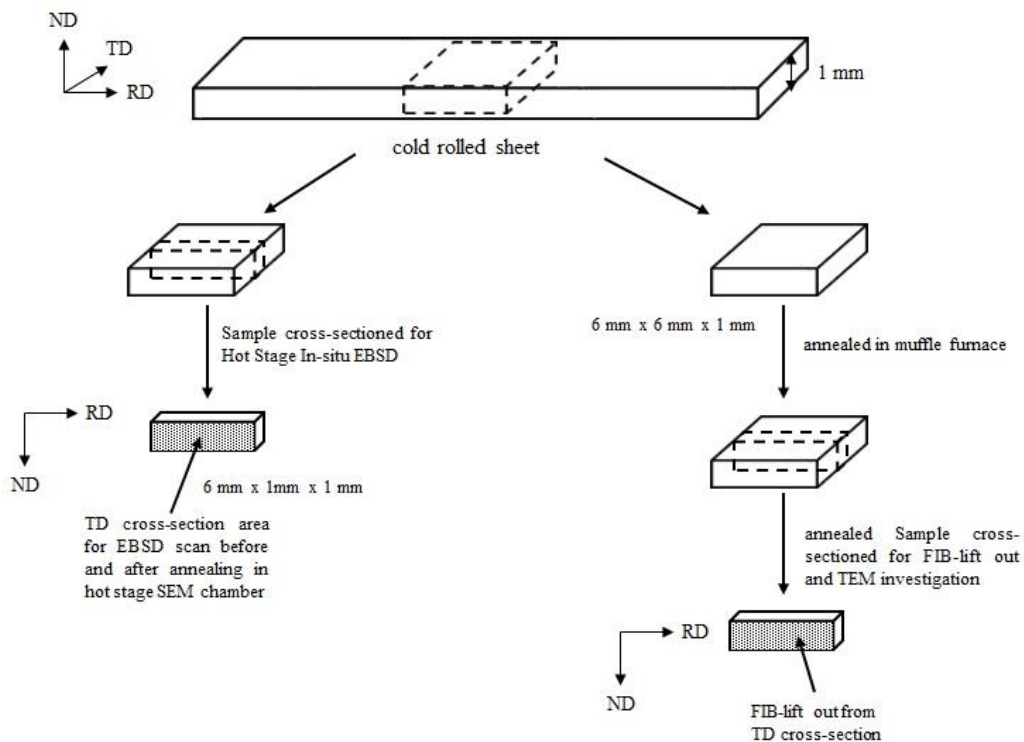


Fig. 1. Sample geometry for Hot Stage *quasi* In-situ EBSD (left) and FIB-lift out TEM (right) investigation.

2.2. FIB-lift out and TEM investigation of furnace-annealed steel

To correlate the *quasi* in-situ EBSD results with the typical bulk-annealing behaviour and to avoid possible decarburization affecting negatively precipitation in the surface layer [50], additional samples

were annealed in a muffle furnace under the same annealing conditions as in the hot-stage *quasi* in-situ EBSD. Samples with dimensions of 6 x 6 x 1 mm were cut from the centre of the as-received sheet and annealed in a muffle furnace for three conditions, 700 °C for 0 s, 800 °C for 0 s and 800 °C for 2 min at a heating rate of ~10 °C/s as mentioned previously. After annealing, the samples were cut in half parallel to the RD-ND plane and polished using the same procedures as mentioned above and then used for FIB lift-out TEM sample preparation. Fig. 1 schematically shows the sample geometry for hot-stage *quasi* in-situ EBSD and furnace-annealing experiments.

Site-specific FIB lift-outs from recrystallized and un-recrystallized regions were carried out to prepare thin samples with dimension of 6 µm x 6 µm and 0.15 µm to 0.2 µm thickness for TEM precipitate investigation. A modified FIB-lift out method was implemented using initial ion milling at 30 kV by Gallium (Ga) ions followed by ion milling at 500 V at an angle of 12° on both sides of the FIB-lift out samples to minimise Ga ion damage and re-deposition [51,52]. Thinned samples were attached to a Copper grid and moved to the FEG-TEM FEI Talos F200X operating at 200 kV. Complex precipitates of Titanium-Vanadium carbides (Ti,V)C were identified from high-resolution scanning-transmission electron microscopy (STEM) imaging and chemical maps were obtained using four EDS Super-X Silicon Drift Detectors (SDD) fitted inside the TEM Talos at a collection angle of 0.9 srad [52]. For image analysis, STEM-EDS chemical maps were imported into the ImageJ software [53] for quantitative analysis of precipitates [54]. For this quantitative analysis, a minimum of 500 precipitates were analysed from 10 different STEM images taken from two different FIB-lift out samples for each annealing condition [52]. Precipitates were assumed to be circular (in 2D) for quantitative analysis [39,55].

2.3. Texture study of bulk furnace-annealed sample using EBSD

Muffle furnace-annealed bulk samples were also used to study the alpha and gamma fibre texture before and after annealing. In order to study texture at large, statistically significant microstructural area, EBSD scans at low magnification of x250 were taken on the RD-ND plane of as-received and annealed samples for three different annealing conditions using the same EBSD data acquisition parameters as mentioned in section 2.1. To achieve representative texture analysis, at least 1000 recrystallized grains in partially recrystallized samples were analysed [56]. EBSD files were exported into HKL Channel 5 software of Oxford Instruments to evaluate Orientation Distribution Function (ODF) on the section $\varphi_2 = 45^\circ$ plotted using Bunge notation [57] for Euler space representation. For cold-rolled and 700 °C 0 s annealed samples, ODF plots were obtained by selecting the complete microstructural matrix. For 800 °C 0 s and 800 °C 2 min annealed samples, ODF plots were obtained by selecting un-recrystallized and recrystallized microstructural matrix respectively [58]. Microstructural matrix with local average misorientation < 1° were characterised as recrystallized grains [59] during selection procedure. Further Vickers hardness measurements were carried out on cold-rolled and muffle furnace-annealed bulk

samples to analyse the hardness contribution from solid solution strengthening of ferrite matrix, precipitation strengthening, dislocation strengthening and grain size strengthening by carrying out 20 indents randomly across the surface using Wilson® VH3300 Automatic Hardness Tester by applying 1000 g load for dwell time of 10 s.

3. Results

3.1. As-received cold-rolled state

Fig. 2 shows a Normal Direction Inverse Pole Figure (ND-IPF) map of the cold-rolled (as-received) state of microalloyed steel. Due to heavy deformation of 70 % with a reduction in thickness to 1 mm, two distinct fibres, alpha ($\langle 110 \rangle // \text{RD}$) and gamma ($\langle 111 \rangle // \text{ND}$) are formed. Apart from the alpha and gamma fibres, there is also a third type of deformed microstructure, which is neither alpha nor gamma fibre signified by randomly orientated subgrains divided by high angle grain boundaries; these results are in accordance with works published previously [10]. Before annealing, the average GND density and average Stored Energy (SE) of the alpha and gamma fibres were evaluated to understand the difference in kinetics of recrystallization in both fibres during annealing. In the cold-rolled condition, the average GND density and average Stored Energy (SE) values for the gamma fibre are $1.17\text{E}+15 \text{ m}^{-2}$ and 2.60 J/cm^3 respectively which is higher than that of the alpha fibre with values of $7.57\text{E}+14 \text{ m}^{-2}$ and 1.68 J/cm^3 , respectively. Therefore, during annealing it is expected that the kinetics of recrystallization will be higher for the gamma fibre due to higher driving force as discussed further [7,14,25,28–30]. In Fig. 2, alpha fibre grains are not only represented as red colour for grain orientation spread around $\{001\}\langle 110 \rangle$ but also purple (combination of red and blue) colour for grain orientation spread around $\{112\}\langle 110 \rangle$ and blue colour for grain orientation spread around $\{111\}\langle 110 \rangle$ which belongs to both alpha and gamma fibres.

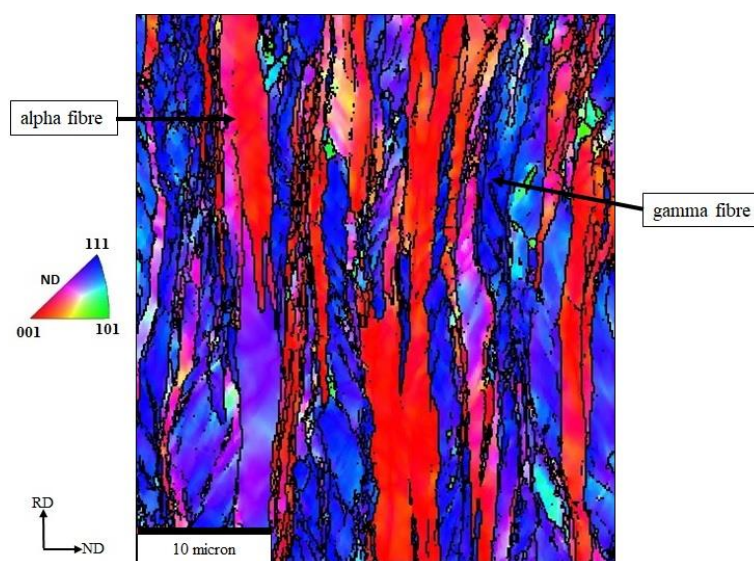


Fig. 2. Normal Direction Inverse Pole Figure (ND-IPF) map of cold-rolled low-carbon microalloyed steel (as-received) for the TD cross-section of the sample. Arrows mark the alpha and gamma fibres in the cold-rolled state.

3.2. Hot stage quasi in-situ EBSD at annealing conditions of 700 °C 0 s; 800 °C 0 s and 800 °C 2 min

Hot-stage EBSD technique is performed to understand the effect of the heating temperature and dwell time on the development of recrystallized texture and recrystallized grain morphology after annealing of cold-rolled low-carbon microalloyed steel. During annealing at a low temperature of 700 °C with no dwell, the microstructure of the annealed sample resembles that of the cold-rolled sample and there are no significant changes in the microstructure and texture. Initiation of nucleation of recrystallization has started in few places as indicated by arrows **A**, **B** and **C** in IPF map of Fig. 3b. The arrow marked **A** has grain orientation $\{112\}\langle 110\rangle$ of the alpha fibre texture and nucleation occurred from a deformed matrix with similar orientation. The arrow marked **B** has grain orientation $\{111\}\langle 110\rangle$ of the gamma fibre texture and nucleation is expected to be linked with the gamma fibre orientation due to its higher initial stored energy. Apart from nucleation of grains with alpha and gamma fibre orientations, some other grains with different orientations such as grain orientation $\{313\}\langle 031\rangle$ marked as **C** have also nucleated from the deformed region surrounded by high-angle grain boundaries. The above grain nucleation characteristics are consistent with the results of Thomas et al. [10] obtained after annealing of IF steel.

At a higher magnification, the bulging of alpha fibre texture grain boundary to the deformed matrix of gamma fibre texture is observed. The average GND density has been calculated for the regions **1**, **2** and **3** in Fig. 3 by capturing the average misorientation value from about 50 pixels. It was found that the average GND density value of region **1** is less than that of region **2** and that the difference in average GND density value between both the regions is about $1.4\text{E}+14\text{ m}^{-2}$. Because of the difference in average GND density and stored energy, high-angle grain boundaries from low average GND regions of the deformed alpha fibre have migrated to the high average GND density regions of deformed gamma fibre, decreasing the average GND density value from $1.4\text{E}+15\text{ m}^{-2}$ to $1.1\text{E}+15\text{ m}^{-2}$ in region **3**. In a previous study on carbon steels by H. Réglé, bulging of subgrain boundaries into gamma grain boundaries has been observed and related to differences in recovery rate and subgrain size [60,61]. In the magnified ND-IPF images of regions **1**, **2** and **3** in Fig. 3 black dots are non-indexed points due to the noise which results from the heavy cold-rolling deformation (about 70 % thickness reduction) and possibly the minor damage of the sample during preparation. The black lines correspond with high-angle grain boundaries ($> 10^\circ$) separating the alpha and gamma fibres.

With an increase in temperature and dwell time to 800 °C 0s and 800 °C 2min, the recrystallization process is initiated and the recrystallization fraction is increased as shown qualitatively by the ND-IPF maps in Fig. 4. Since the gamma fibre has a higher initial stored energy (driving force for recrystallization) as compared to alpha fibre in cold rolled state, therefore during annealing it could be

observed from ND-IPF maps in Fig. 4c and Fig. 4d that the alpha fibre is still in recovery stage while grains belonging to the gamma fibre are fully recrystallized and the stored energy is released lowering the GND density. Site specific local average misorientation, GND density and Stored Energy (SE) maps are shown from the matrix of alpha, gamma, and other orientations. After annealing at 800 °C 0s, average GND density values in region **1'** (grain orientation spread around $\{001\}\langle 110\rangle$) and **2'** (grain orientation spread around $\{112\}\langle 110\rangle$) of the un-recrystallized alpha fibre are $6.1\text{E}+14\text{ m}^{-2}$ and $2.0\text{E}+14\text{ m}^{-2}$ respectively, which decreased as compared to the as-received average GND values in region **1** and **2** of $6.2\text{E}+14\text{ m}^{-2}$ and $2.3\text{E}+14\text{ m}^{-2}$, as shown in Fig. 4a and Fig. 4c respectively. While in the case of recrystallized grain **3'** (grain orientation $\{111\}\langle 110\rangle$ of gamma fibre texture), recrystallized grain **4'** (grain orientation $\{123\}\langle 121\rangle$) and recrystallized grain **5'** (grain orientation $\{313\}\langle 031\rangle$) the average GND density values are $2.3\text{E}+13\text{ m}^{-2}$, $3.2\text{E}+13\text{ m}^{-2}$ and $4.0\text{E}+13\text{ m}^{-2}$ respectively. Qualitatively and from the average GND values, drop in the stored energy has not taken place much in the un-recrystallized alpha fibre matrix and therefore un-recrystallized grains belonging to alpha fibre have potential for further recrystallization during increment of dwell time by 2 min for 800 °C.

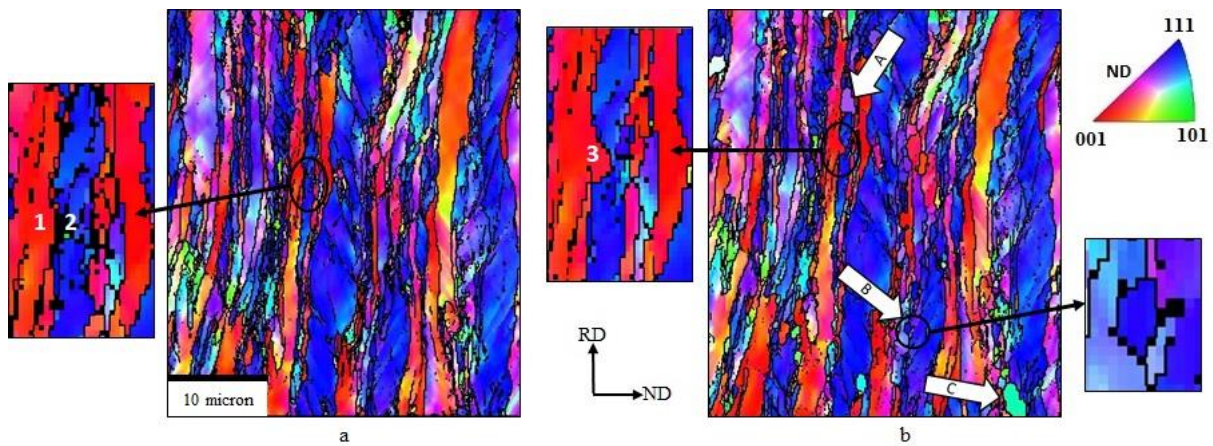


Fig. 3. Normal Direction Inverse Pole Figure (ND-IPF) maps of low-carbon micro-alloyed steel before annealing (a) and after annealing at 700 °C 0 s (b). In Fig. 3a, the alpha fibre region is marked as **1** and the gamma fibre region is marked as **2** for the cold-rolled state. In Fig. 3b, a bulged portion of the alpha fibre region is marked as **3** for the annealed sample. Arrows marked as **A**, **B** and **C** in Fig. 3b are recrystallized nucleus after annealing.

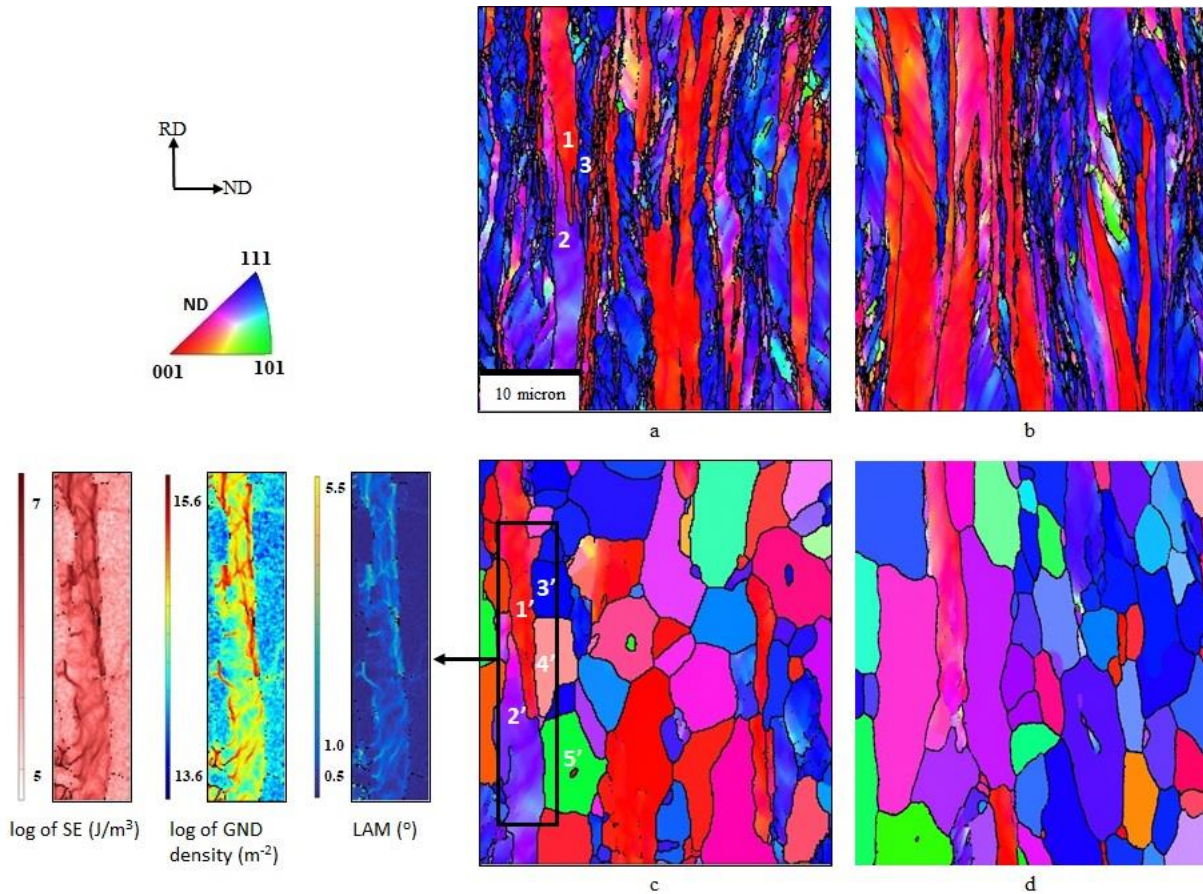


Fig. 4. Normal Direction Inverse Pole Figure (ND-IPF) maps for two annealing conditions: before (a) and after (c) annealing at 800 °C 0 s, and before (b) and after (d) annealing at 800 °C 2 min. For 800 °C 0 s annealing condition, site specific local average misorientation (LAM), log of geometrically necessary dislocation (GND) density and log of stored energy (SE) map is shown for the un-recrystallized and recrystallized matrix of annealed sample.

3.3. Precipitation study

For temperature of 700 °C with no dwell, fine precipitates of (Ti,V)C ($d < 15$ nm) are found to form in the un-recrystallized deformed bands and on recovered sub-grain boundaries and provide resistance to boundary motion by Zener pinning during annealing [62] as shown in bright field (BF) and EDS chemical map of Fig. 5. With increase in temperature to 800 °C and dwell time from 0 s to 2 min, counts (%) of coarse precipitates ($d > 15$ nm) is increased as shown in the Fig. 6b. Because of the increased temperature, dwell time and the fact that precipitates are coarser, grain boundaries are able to move [62] and the deformed grains and bands are recrystallized into fully grown strain free grains. For annealing condition of 800 °C 2 min, both fine ($d < 15$ nm) and coarse ($d > 15$ nm) precipitates are present in recrystallized ferrite grain as illustrated in a bright field (BF) image shown in Fig. 6a. The data in Fig. 6b shows that counts (%) of finer precipitates ($d < 15$ nm) are higher for 700 °C 0 s and 800 °C 0 s and counts (%) of coarser precipitates ($d > 15$ nm) are higher for 800 °C 2 min. The average diameter of

precipitates of 700 °C 0 s, 800 °C 0 s and 800 °C 2 min are 11.2 ± 5.2 nm, 12.0 ± 5.5 nm and 13.6 ± 6.4 nm respectively.

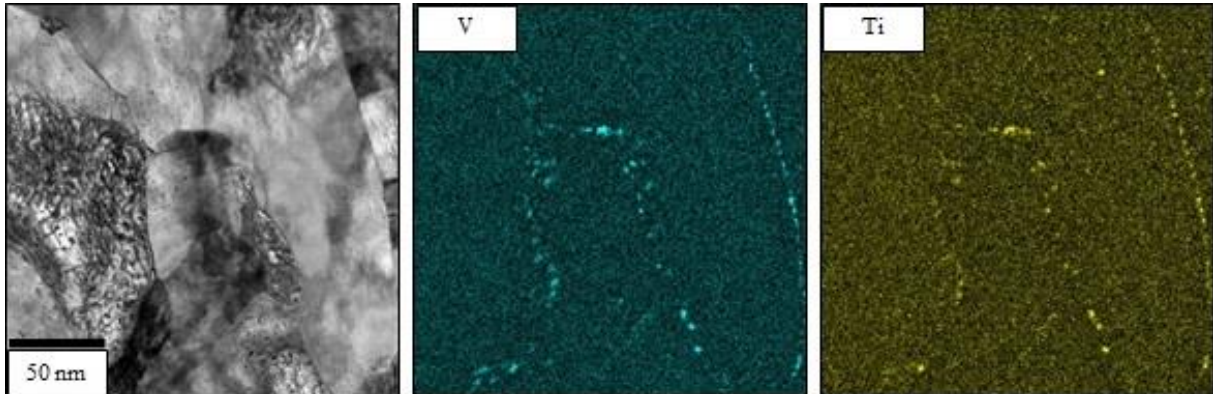


Fig. 5. STEM bright field (BF) image and EDS chemical map of carbides of Titanium and Vanadium (Ti,V)C precipitates pinned to a sub-grain boundary at 700 °C 0 s for low-carbon micro-alloyed steel at two different FIB-lift out samples after bulk-furnace annealing.

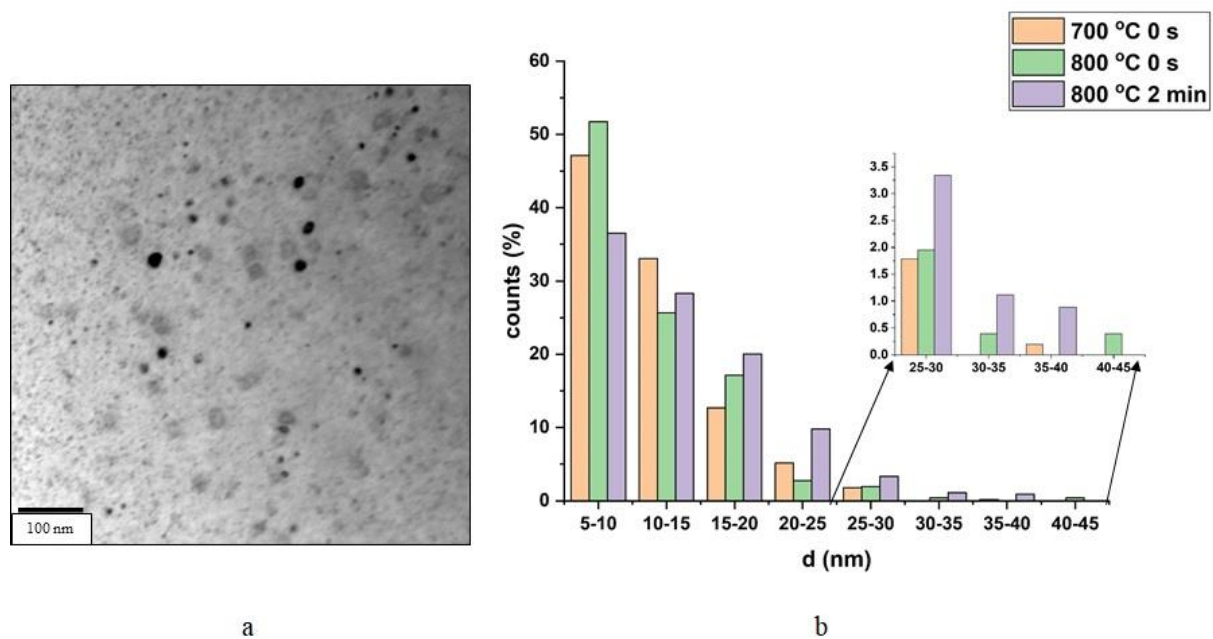


Fig. 6. STEM bright field (BF) image (a) of carbides of Titanium and Vanadium (Ti,V)C precipitates present inside recrystallized grains for annealing condition of 800 °C 2 min and counts (%) versus precipitate size plot (b) for three different annealing conditions for low carbon micro-alloyed steel.

3.4. Role of alpha and gamma fibres during annealing

In order to further understand the difference in change in average GND density in un-recrystallized and recrystallized portions of alpha and gamma fibres and its role on the recrystallization mechanism at different annealing conditions, average GND density and recrystallization (%) are calculated and plotted for respective fibres [59]. In Fig. 7a it can be observed that the average GND density is higher

in un-recrystallized portion as compared to recrystallized region. For annealing condition of 700 °C 0 s, decrease in average GND density is higher in un-recrystallized gamma fibre texture ($3.0E+14 \text{ m}^{-2}$) as compared to un-recrystallized alpha fibre texture ($1.1E+14 \text{ m}^{-2}$). With further increase in temperature to 800 °C and dwell time from 0 s to 2 min, average GND density decreases due to static recovery. The drop in average GND density is higher for un-recrystallized gamma fibre grains ($6.2E+14 \text{ m}^{-2}$ for 800 °C 0 s and $9.8E+14 \text{ m}^{-2}$ for 800 °C 2 min) than for un-recrystallized alpha fibre grains ($1.4E+14 \text{ m}^{-2}$ for 800 °C 0s and $4.5E+14 \text{ m}^{-2}$ for 800 °C 2 min). The smaller drop in the mean GND density of un-recrystallized alpha fibre from cold rolled state to annealed state at 700 °C 0 s , 800 °C 0 s and 800 °C 2 min in Fig. 7a indicates that the extent of static recovery is negligible in this fibre. But the results of larger drop in mean GND density for un-recrystallized gamma fibre imply that static recovery is much faster and readily occurred even at annealing state 700 °C 0 s. For recrystallized grains of alpha and gamma fibre orientation, average GND density value is about $4.5E+13 \text{ m}^{-2}$, which is as expected considerably lower than for un-recrystallized matrix.

Similarly with increase in the heat input from 700 °C 0 s to 800 °C 2 min, recrystallization (%) for both fibres have increased. From qualitative ND-IPF maps in Fig. 4 and quantitative average GND (m^{-2}) density and recrystallization (%) results shown in Fig. 7a and Fig. 7b respectively, it could be observed that due to the higher initial stored energy in the cold-rolled gamma fibre, as compared to the cold-rolled alpha fibre, drop in the average GND density and increase in the recrystallization fraction (%) is higher in the case of gamma fibre grains. Annealing at 800 °C with increase in dwell time from 0 s to 2 min results in negligible increment in recrystallization (%) (from 70 % to 72 %) for alpha fibre grains, while for gamma fibre grains increment in recrystallization (%) is significant (from 73 % to 93 %). The above measured recrystallized fractions in alpha and gamma fibres imply that fine precipitates of (Ti,V)C probably pinned recrystallized alpha grains from 0 s to 2 min at 800 °C, whilst they cannot stop the recrystallization behaviour of gamma fibre grains.

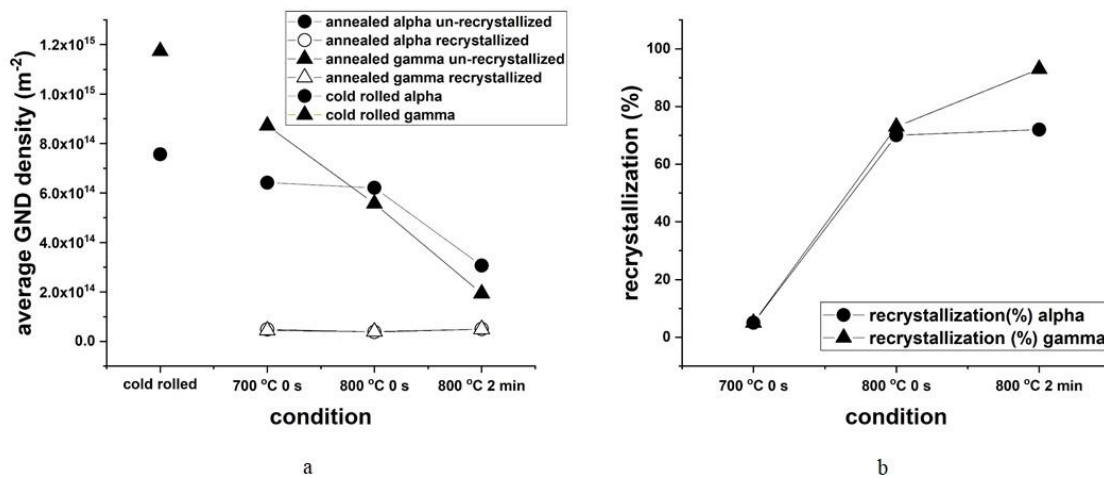


Fig. 7. Average GND density plot for cold-rolled alpha and gamma fibres and recrystallized and un-recrystallized matrix (grains) of alpha and gamma fibres at different annealing conditions (a). Fig. 7b shows recrystallization (%) of alpha and gamma matrix (grains) at different annealing conditions for low-carbon micro-alloyed steel.

Further, overall recrystallization for three different annealing conditions, 700 °C 0 s, 800 °C 0 s and 800 °C 2 min is evaluated using local average misorientation (LAM) map with an example shown in Fig.8. With an increase in temperature and dwell time, recrystallization (%) increases (6 % for 700 °C 0 s; 75 % for 800 °C 0 s; 91 % for 800 °C 2 min), and because of softening, average hardness (HV/1) decreases from 280 to 190 HV number as shown in Fig.9. With increase in temperature and dwell time dislocation density (in present case GND density) decreases and leads to softening [63].

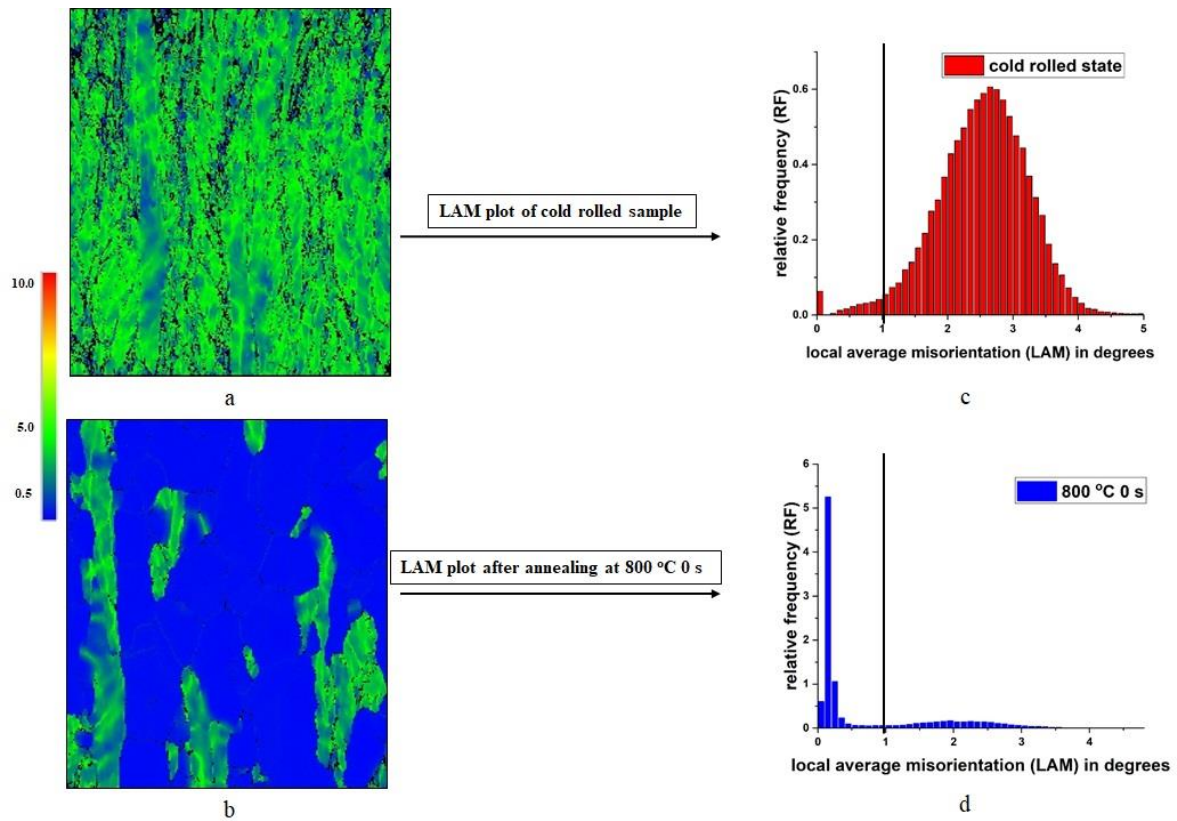


Fig. 8. Local average misorientation (LAM) map (a) and (b) and plots (c) and (d) before and after annealing of low-carbon micro-alloyed steel at 800 °C 0 s.

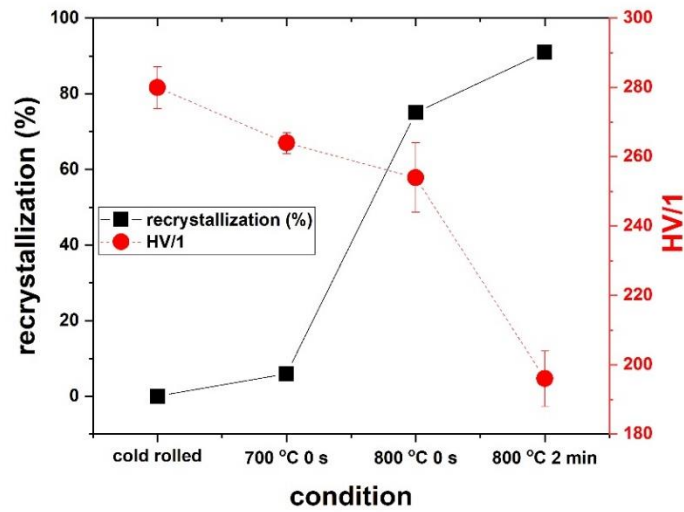


Fig. 9 Fraction recrystallized (%) and Vickers hardness (HV at force of 1 kgf) plots for cold-rolled state and annealed samples obtained at different annealing conditions.

3.5. Texture analysis of bulk annealed samples

In the case of cold rolled low carbon steel, both alpha and gamma fibres are dominant with maximum orientation densities of 10.92 and 10.60 respectively as shown in Fig. 10a. Alpha fibre has maximum orientation density peak at $\{112\}\langle 110\rangle$ grain [64]. Gamma fibre texture has the maximum orientation density peak at $\{111\}\langle 110\rangle$ grain rather than $\{111\}\langle 112\rangle$ grain, which is shown as the characteristics of low carbon steel deformed between 70 % and 80 % by Hölscher et al. using their “pancake” mathematical modelling [65]. To further understand the development of recrystallized texture, ODF plots were evaluated for un-recrystallized and recrystallized matrix for different annealing conditions. As has been shown in Fig. 3 complete recrystallization has not taken place in the sample annealed at 700 °C 0 s and only limited nucleation occurred with the presence of about ~95% of as-deformed matrix, therefore texture of the complete matrix (un-recrystallized and recrystallized) of annealed steel is evaluated and it is found to be similar to the cold rolled (as-received) steel texture as shown in Fig. 10a and 10b. In case of recrystallized matrix, for annealing condition of 800 °C 0 s and 800 °C 2 min, maximum orientation density peak is at around $\{111\}\langle 110\rangle$ grain in alpha fibre as compared to the peak at $\{112\}\langle 110\rangle$ grain in cold-rolled condition. Also, with increase in dwell time from 0 s to 2 min at the temperature of 800 °C, the strength of gamma fibre is increased in recrystallized matrix as shown in Fig. 10d and 10f, while the texture for un-recrystallized matrix is similar to that of cold-rolled steel with the presence of alpha and gamma fibre as shown in Fig. 10c and 10e.

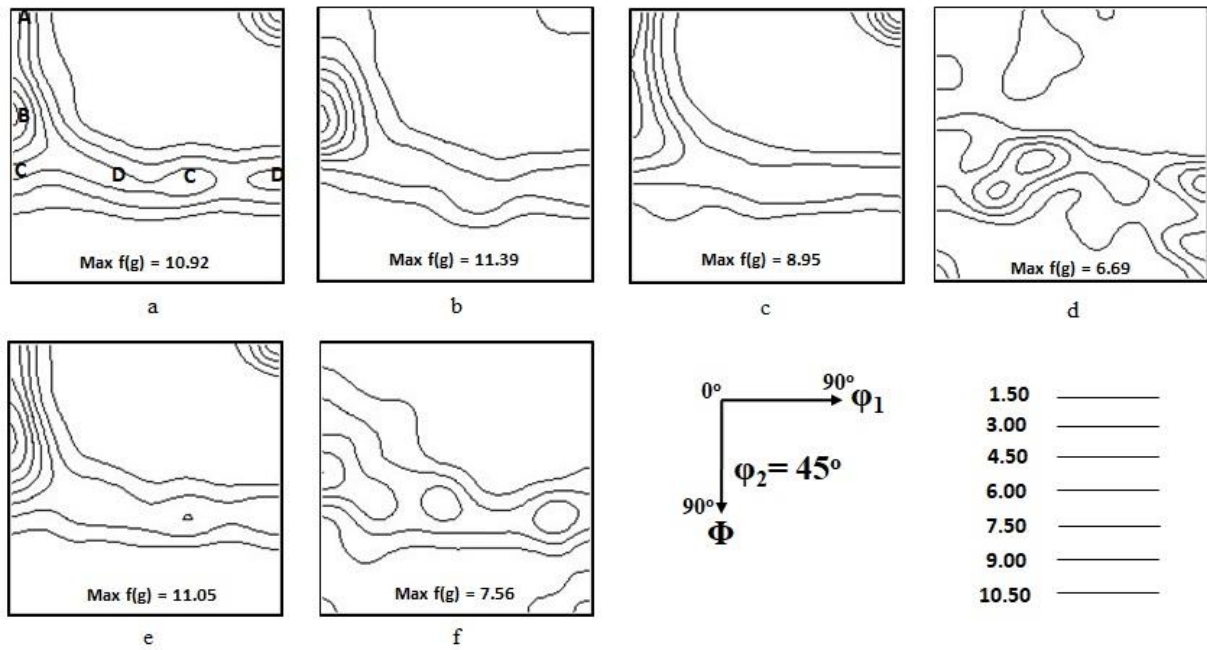


Fig. 10. ODF on the section $\phi_2 = 45^\circ$: cold rolling texture for as-received state (a), complete texture for both un-recrystallized and recrystallized matrix after annealing at 700 °C 0 s (b), texture for un-recrystallized matrix after annealing at 800 °C 0 s (c), texture for recrystallized matrix after annealing at 800 °C 0 s (d), texture for un-recrystallized matrix after annealing at 800 °C 2 min (e) and texture for recrystallized matrix after annealing at 800 °C 2 min (f). A = {001}<110>; B = {121}<110>; C = {111}<110> and D = {111}<121> grain orientation.

4. Discussion

4.1. Reliability of surface microstructural observation for hot stage quasi in-situ EBSD sample

Since the surrounding boundary conditions of free surface microstructure are different from the interior bulk microstructure, such as that the surface microstructure is exposed to a gas (of pressure, $P \sim 5 \times 10^{-6}$ mbar) inside the SEM chamber [66], therefore it is important to discuss the differences or similarities in recrystallized microstructure development on the surface and in the interior of the sample for the same annealing conditions. To investigate the above case, hot stage *quasi* in-situ EBSD samples were polished down to $\sim 300 \mu\text{m}$ along transverse direction (TD) and high magnification (x5k) EBSD scans were performed on annealed samples. Microstructure on the surface and in the interior of the hot stage *quasi* in-situ EBSD sample is very similar qualitatively to each other after annealing for three different conditions, 700 °C 0 s, 800 °C 0 s and 800 °C 2 min as shown in Fig. 3b; 4c and 4d (surface) and Fig. 11a; 11b and 11c (interior) respectively. Recrystallized grains are quasi-polygonal for both surface and interior of annealed samples. For annealing condition of 700 °C 0 s, not much nucleation could be observed even inside the sample as shown in Fig. 11a, which further confirms annealing temperature of 700 °C with no dwell is not sufficient for complete recrystallization. Presence of un-recrystallized alpha fibre grains for annealing conditions of 800 °C 0 s and 800 °C 2 min in Figs. 11b and 11c respectively confirms that the slower recrystallization kinetics of the alpha fibre grains is not only observed on the

surface but also inside the bulk. Samajdar et al. [67,68] and Sinclair et al. [61] had defined the recrystallization behaviour of alpha fibre grains as “sluggish”. Samajdar investigated IF steel and Sinclair investigated ferritic stainless steel and both of them observed the slow kinetics of recrystallization in case of alpha fibre grains. Grain $\{001\}\langle 110\rangle$ and $\{112\}\langle 110\rangle$ belong to alpha fibre and have less stored energy as compared to grain $\{111\}\langle 110\rangle$ and grain $\{111\}\langle 112\rangle$ which belong to gamma fibre [9,30]. This difference in stored energy gives the advantage to gamma fibre for higher nucleation kinetics which further leads to the preferential growth of gamma fibre subgrains and to higher recrystallization fraction as compared to alpha fibre grains [67]. Another reason for the slower recrystallization kinetics of alpha fibre grains is related to the lattice curvature. Regions of sharp lattice curvature facilitates nucleation for recrystallization due to higher misorientations ($>15^\circ$). In cold-rolled low carbon steel, alpha fibre grains lack the sharp lattice curvature as compared to gamma fibre grains and therefore form much less potential sites for nucleation during annealing [69,70].

Since qualitatively there is not any significant effect of the free surface on the recrystallized microstructural development, therefore to further understand quantitatively the difference in recrystallized microstructure on the surface and in the interior, recrystallization (%) and average recrystallized grain size are plotted as shown in Figs. 11d and 11e respectively. Average recrystallized grain size on surface is **about 1.2 to 1.6 times coarser as compared** to the interior of the sample for same annealing conditions. Average recrystallization (%) is higher by 5 % for surface as compared to interior of the sample for annealing condition of 800 °C 0 s and 800 °C 2 min. From the above quantified results, it could be seen that the values for recrystallization (%) and grain size are within the standard deviation for the surface and the interior but with a slight increase in average values for the surface, possibly due to the following factors: easier shape deformation on the free surface as compared to the bulk [46,71], temperature gradient from surface to interior, the free surface energy [14,66], **or absence of recrystallized grains which nucleate above the free surface [17,21,72,73]**. Mullins had previously discussed the effect of free surface on grain growth, and it was mentioned that as the surface microstructures are exposed to the gas, therefore there are various free surface energies associated with grain boundary movement. Grain of higher surface free energy could be consumed by grain of lower free surface energy and lead to grain coarsening [66]. **Moreover, during annealing using hot stage EBSD most of the recrystallized nuclei are formed below the surface and almost half of the recrystallized grains emerge from below to reach the free surface [17,21,72,73]**. Therefore, by the end of the annealing process, the number of recrystallized grains on surface would be statistically half as many as interior. Hence, average recrystallized grain area on the surface would be almost double as compared to the interior, and the average recrystallized grain size about 1.4 times larger than the recrystallized grain size in the interior, which also agrees with the results shown in Fig. 11e. Overall, from both **qualitative and quantitative results**, we did not see any significant deviation in recrystallized

microstructural development on the surface and in the interior of the annealed sample, which is consistent with the observations from other researchers [14,21].

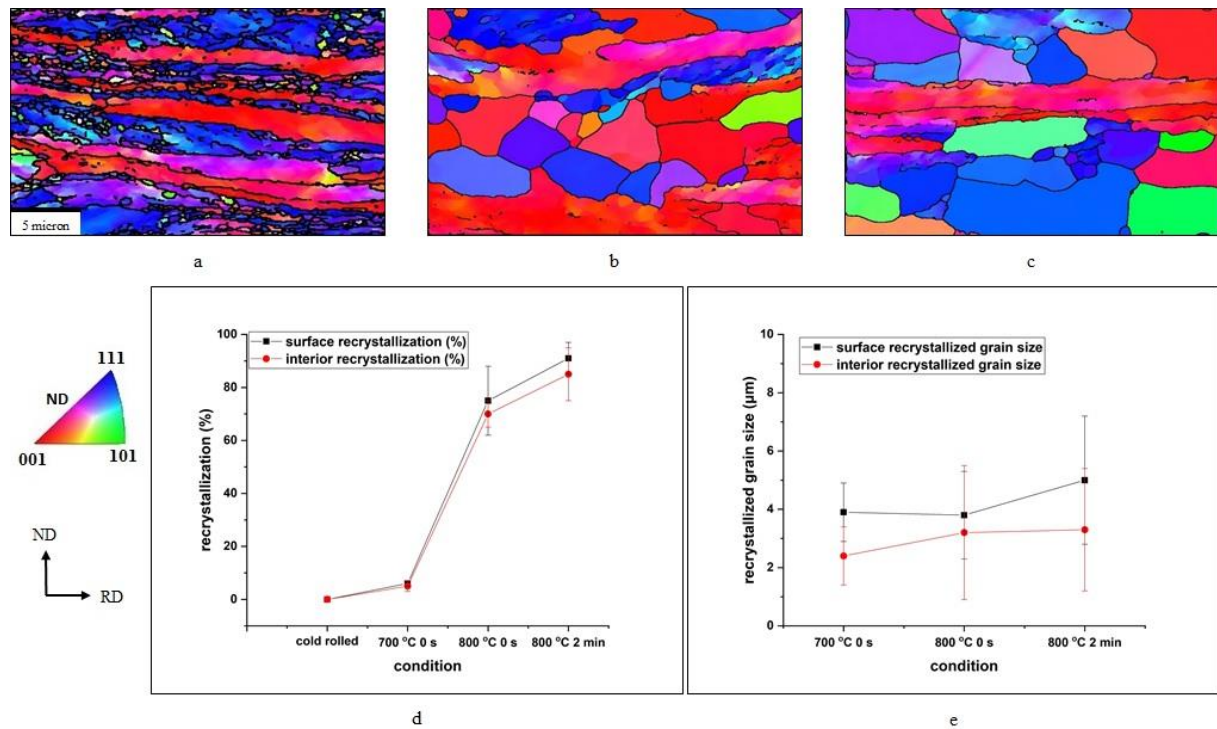


Fig. 11. Normal Direction Inverse Pole Figure (ND-IPF) maps of interior microstructure of hot stage *quasi* in-situ samples for three annealing conditions: 700 °C 0 s (a), 800 °C 0 s (b) and 800 °C 2 min (c). Fraction recrystallized (%) (d) and recrystallized grain size (μm) (e) quantified on surface and interior microstructure of hot stage *quasi* in-situ samples for cold-rolled state and annealed states obtained at different annealing conditions.

4.2. Development of texture in bulk annealed samples

During cold rolling, grains in polycrystals undergo rotation from less stable orientation towards more stable orientation to form texture [74,75]. The cold rolling texture of the investigated composition mainly consists of alpha and gamma fibres with the ODF density peaks at around $\{112\}\langle 110\rangle$ and $\{111\}\langle 110\rangle$. This texture is very similar to the typical cold rolling texture observed in body centred cubic metals. For annealing conditions of 800 °C 0 s and 800 °C 2 min, subgrain growth mechanism favours preferential nucleation of high stored energy gamma fibre grains [25], which could be the possible reason for the strengthening of gamma fibre in recrystallized region as shown in Fig. 10d and 10f. Similarly in the case of alpha fibre grains, preferential nucleation takes place in higher stored energy grain, $\{111\}\langle 110\rangle$ [30] and thus allows it to grow further in the competitive process of annealing [30,76]. The above competition between different alpha fibre grains results in drop in area (%) of $\{112\}\langle 110\rangle$ and $\{001\}\langle 110\rangle$ grains from ~27 % and ~11.8 % in cold-rolled state to ~7.5 % and ~1.4% in annealed state for 800 °C 0 s and to ~10% and ~3.9% in annealed state for 800 °C 2 min respectively.

From above results and discussions, it could be found that hot stage *quasi* in-situ EBSD is an important tool for studying recrystallized texture development and the microstructure of the annealed steel sample. Also evaluating the initial stored energy from the contribution of GND density for alpha and gamma fibre grains gives a clear indication of the difference in kinetics of recrystallization in respective fibres. In future, neutron diffraction methodology [77] could be implemented to study the contribution of SSD and GND for complete evaluation of stored energy in respective fibres [32]. Additional high resolution TEM/STEM study coupled with EBSD to study the preferential growth of precipitates on respective alpha and gamma fibres and to understand interaction with dislocations during annealing is currently in progress and will be published separately.

5. Conclusions

- Evaluating average GND density from same region indicates a slower recovery rate in alpha fibre than in gamma fibre for the annealing conditions of 700 °C 0 s, 800 °C 0 s and 800 °C 2 min.
- In this study, there is no significant difference in microstructure on surface and interior of hot stage *quasi* in-situ EBSD annealed samples, but average recrystallized fraction is slightly higher on sample surface than in sample interiors.
- At the lower annealing temperature of 700 °C with no dwell, nucleation of recrystallization has initiated both on surface and interior of hot stage *quasi* in-situ annealed sample but the temperature and dwell time are not sufficient for full recovery and recrystallization. With longer dwell time (> 2 min) at 800 °C recrystallization has progressed with higher recrystallization fraction in gamma fibre grains as compared to alpha fibre grains. The minor increase in the recrystallized fraction of alpha fibre from 0s to 2 min at 800 °C implies that fine precipitates probably pinned recrystallized grains. The pinning force however did not stop the recrystallization behaviour of gamma fibre grains. Moreover due to lower stored energy and lack of sharp lattice curvature in alpha fibre, recovery and recrystallization time is longer for alpha fibre than for gamma fibre.
- Cold-rolled low carbon micro-alloyed steel has strong alpha and gamma fibres in the as-received state. During annealing, the un-recrystallized region resembles cold-rolled texture while the recrystallized region has strong gamma fibre due to preferential nucleation of higher stored energy gamma fibre grains.

Acknowledgements

Authors are thankful to Tata Steel Europe for providing experimental materials and giving technical guidance. For experiments, thanks to Dr Geoff West from Advanced Materials and Manufacturing Centre, WMG for technical guidance in preparing STEM sample via FIB-lift out, Dr Hiren Kotadia for technical guidance in operating muffle furnace and Mr Samuel Clark, who was final year PhD Student

in WMG for guidance in usage of MTEX-4.5.0 toolbox available in MATLAB 2016b. Financial assistance from WMG departmental scholarship for Mr Ishwar Kapoor is gratefully acknowledged and Dr Zushu Li would like to thank the financial support from EPSRC (EP/N011368/1).

Data availability

The raw/processed data required to reproduce these findings cannot be shared at this time due to technical or time limitations.

References

- [1] D. Raabe, 23 - Recovery and Recrystallization: Phenomena, Physics, Models, Simulation, in: D.E. Laughlin, K. Hono (Eds.), *Phys. Metall.*, Fifth Edit, Elsevier, Oxford, 2014: pp. 2291–2397. doi:10.1016/B978-0-444-53770-6.00023-X.
- [2] R.D. Doherty, D.A. Hughes, F.J. Humphreys, J.J. Jonas, D.J. Jensen, M.E. Kassner, W.E. King, T.R. Mcnelley, H.J. Mcqueen, A.D. Rollett, Current issues in recrystallization: a review, *Mater. Sci. Eng. A.* 238 (1997) 219–274. doi:10.1016/S0921-5093(97)00424-3.
- [3] B. Hutchinson, Deformation microstructures and textures in steels, *Philos. Trans. R. Soc. London. Ser. A Math. Phys. Eng. Sci.* 357 (1999) 1471–1485. doi:10.1098/rsta.1999.0385.
- [4] R. Grimes, R. Dashwood, H. Flower, Processing of high superplastic strain rate aluminium alloys, *Alum. Int. Today.* 15 (2003) 64–66. https://www.researchgate.net/publication/286768514_Processing_of_high_superplastic_strain_rate_aluminium_alloys.
- [5] I. Kapoor, R.G. Narayanan, S. Taylor, V. Janik, R. Dashwood, Predicting the Warm Forming Behavior of WE43 and AA5086 Alloys, in: *Procedia Eng.*, 2017: pp. 897–904. doi:10.1016/j.proeng.2016.12.136.
- [6] N. Gope, D.K. Rout, S. Mukherjee, G. Jha, A.N. Bhagat, A.K. Verma, D. Bhattacharjee, A.K. Srivastava, High Strength Steels for Automotive applications: Recent Trends and Experience at Tata Steel, *SAE Trans.* 26 (2005) 333–344. doi:10.4271/2005-26-333.
- [7] G. Bhargava, L. Patra, S. Pai, D. Mishra, A Study on Microstructure, Texture and Precipitation Evolution at Different Stages of Steel Processing in Interstitial Free High Strength Steels, *Trans. Indian Inst. Met.* 70 (2017) 631–637. doi:10.1007/s12666-017-1089-7.
- [8] H. Bhadeshia, R. Honeycombe, *Steels: Microstructure and Properties*, 4th ed., Butterworth-Heinemann, Great Britain, 2011.
- [9] R.K. Ray, J.J. Jonas, R.E. Hook, Cold rolling and annealing textures in low carbon and extra low carbon steels, *Int. Mater. Rev.* 39 (1994) 129–172. doi:10.1179/imr.1994.39.4.129.
- [10] I. Thomas, S. Zaefferer, F. Friedel, D. Raabe, High-Resolution EBSD Investigation of Deformed and Partially Recrystallized IF Steel, *Adv. Eng. Mater.* 5 (2003) 566–570. doi:10.1002/adem.200300373.
- [11] S.-H. Hong, D.N. Lee, Grain coarsening in IF steel during strain annealing, *Mater. Sci. Eng. A.* 357 (2003) 75–85. doi:10.1016/S0921-5093(03)00257-0.
- [12] H.S. Ubhi, J. Parsons, N. Othen, S. Campbell, R. Poole, A. Gholinia, In-situ EBSD Phase Transformation and Recrystallisation, in: *J. Phys. Conf. Ser.*, 2014: p. 12011. doi:10.1088/1742-6596/522/1/012011.

- [13] S. Tokita, H. Kokawa, Y.S. Sato, H.T. Fujii, In situ EBSD observation of grain boundary character distribution evolution during thermomechanical process used for grain boundary engineering of 304 austenitic stainless steel, *Mater. Charact.* 131 (2017) 31–38. doi:10.1016/j.matchar.2017.06.032.
- [14] H. NAKAMICHI, F.J. HUMPHREYS, I. BROUGH, Recrystallization phenomena in an IF steel observed by in situ EBSD experiments, *J. Microsc.* 230 (2008) 464–471. doi:10.1111/j.1365-2818.2008.02006.x.
- [15] V. Janik, S. Clark, P. Srirangam, A. Rijkenberg, S. Seetharaman, Application of In-Situ Material Characterization Methods to Describe Role of Mo During Processing of V-Bearing Micro-Alloyed Steels, in: *HSLA Steels 2015, Microalloying 2015* {&} *Offshore Eng. Steels 2015*, Springer International Publishing, Cham, 2016: pp. 289–295. doi:10.1007/978-3-319-48767-0_31.
- [16] Y. Zhang, A. Godfrey, D. Juul Jensen, In-Situ Investigation of Local Boundary Migration During Recrystallization, *Metall. Mater. Trans. A.* 45 (2014) 2899–2905. doi:10.1007/s11661-014-2222-4.
- [17] F. Brisset, A. Helbert, T. Baudin, In Situ Electron Backscatter Diffraction Investigation of Recrystallization in a Copper Wire, *Microsc. Microanal.* 19 (2013) 969–977. doi:10.1017/S1431927613000299.
- [18] D.P. Field, L.T. Bradford, M.M. Nowell, T.M. Lillo, The role of annealing twins during recrystallization of Cu, *Acta Mater.* 55 (2007) 4233–4241. doi:10.1016/j.actamat.2007.03.021.
- [19] N. Bozzolo, S. Jacomet, R.E. Logé, Fast in-situ annealing stage coupled with EBSD: A suitable tool to observe quick recrystallization mechanisms, *Mater. Charact.* 70 (2012) 28–32. doi:10.1016/j.matchar.2012.04.020.
- [20] G.G.E. Seward, D.J. Prior, J. Wheeler, S. Celotto, D.J.M. Halliday, R.S. Paden, M.R. Tye, High-temperature electron backscatter diffraction and scanning electron microscopy imaging techniques: In-situ investigations of dynamic processes, *Scanning.* 24 (2002) 232–240. doi:10.1002/sca.4950240503.
- [21] C. KERISIT, R.E. LOGÉ, S. JACOMET, V. LLORCA, N. BOZZOLO, EBSD coupled to SEM in situ annealing for assessing recrystallization and grain growth mechanisms in pure tantalum, *J. Microsc.* 250 (2013) 189–199. doi:10.1111/jmi.12034.
- [22] D. Guan, W.M. Rainforth, L. Ma, B. Wynne, J. Gao, Twin recrystallization mechanisms and exceptional contribution to texture evolution during annealing in a magnesium alloy, *Acta Mater.* 126 (2017) 132–144. doi:10.1016/j.actamat.2016.12.058.
- [23] D. Guan, W.M. Rainforth, J. Gao, L. Ma, B. Wynne, Individual effect of recrystallisation nucleation sites on texture weakening in a magnesium alloy: Part 2-shear bands, *Acta Mater.* 145 (2018) 399–412. doi:10.1016/j.actamat.2017.12.019.
- [24] P.J. Hurley, F.J. Humphreys, A study of recrystallization in single-phase aluminium using in-situ annealing in the scanning electron microscope, *J. Microsc.* 213 (2004) 225–234. doi:10.1111/j.0022-2720.2004.01300.x.
- [25] I.L. Dillamore, C.J.E. Smith, T.W. Watson, Oriented Nucleation in the Formation of Annealing Textures in Iron, *Met. Sci. J.* 1 (1967) 49–54. doi:10.1179/msc.1967.1.1.49.
- [26] A. Wauthier-Monnin, T. Chauveau, O. Castelnau, H. Réglé, B. Bacroix, The evolution with strain of the stored energy in different texture components of cold-rolled IF steel revealed by high resolution X-ray diffraction, *Mater. Charact.* 104 (2015) 31–41. doi:10.1016/j.matchar.2015.04.005.
- [27] O. Engler, V. Randle, Chapter 5 - Evaluation and Representation of Macrotexture Data, in: *Introd. to Texture Anal. Macrotexture, Microtexture, Orientat. Mapp.*,

- Second, CRC press, Boca Raton, 2009: pp. 123–172.
- [28] S.W. Ooi, G. Fourlaris, A comparative study of precipitation effects in Ti only and Ti–V Ultra Low Carbon (ULC) strip steels, *Mater. Charact.* 56 (2006) 214–226. doi:10.1016/j.matchar.2005.11.010.
- [29] C. Fang, *Annealing and Precipitation Behavior During Batch Annealing of HSLA Steels*, Doctoral Dissertation, University of Pittsburgh, 2011. <http://d-scholarship.pitt.edu/id/eprint/6433>.
- [30] W.B. Hutchinson, Development and control of annealing textures in low-carbon steels, *Int. Met. Rev.* 29 (1984) 25–42. doi:10.1179/imtr.1984.29.1.25.
- [31] M.F. Ashby, The deformation of plastically non-homogeneous materials, *Philos. Mag. A J. Theor. Exp. Appl. Phys.* 21 (1970) 399–424. doi:10.1080/14786437008238426.
- [32] Y.A. Betanda, A.-L. Helbert, F. Brisset, M.-H. Mathon, T. Waeckerlé, T. Baudin, Measurement of stored energy in Fe–48%Ni alloys strongly cold-rolled using three approaches: Neutron diffraction, Dillamore and KAM approaches, *Mater. Sci. Eng. A.* 614 (2014) 193–198. doi:10.1016/j.msea.2014.07.037.
- [33] S. Wright, M. Nowell, D. Field, A Review of Strain Analysis Using Electron Backscatter Diffraction, *Microsc. Microanal.* 17 (2011) 316–329. doi:10.1017/S1431927611000055.
- [34] J. Jiang, T.B. Britton, A.J. Wilkinson, Evolution of dislocation density distributions in copper during tensile deformation, *Acta Mater.* 61 (2013) 7227–7239. doi:10.1016/j.actamat.2013.08.027.
- [35] M. Calcagnotto, D. Ponge, E. Demir, D. Raabe, Orientation gradients and geometrically necessary dislocations in ultrafine grained dual-phase steels studied by 2D and 3D EBSD, *Mater. Sci. Eng. A.* 527 (2010) 2738–2746. doi:10.1016/j.msea.2010.01.004.
- [36] N. Hansen, X. Huang, G. Winther, Grain orientation, deformation microstructure and flow stress, *Mater. Sci. Eng. A.* 494 (2008) 61–67. doi:10.1016/j.msea.2007.10.086.
- [37] L.P. Kubin, A. Mortensen, Geometrically necessary dislocations and strain-gradient plasticity: a few critical issues, *Scr. Mater.* 48 (2003) 119–125. doi:10.1016/S1359-6462(02)00335-4.
- [38] H. Gao, Y. Huang, W.D. Nix, J.W. Hutchinson, Mechanism-based strain gradient plasticity— I. Theory, *J. Mech. Phys. Solids.* 47 (1999) 1239–1263. doi:10.1016/S0022-5096(98)00103-3.
- [39] T. Gladman, *The physical metallurgy of microalloyed steels*, Institute of Materials, London, 1997.
- [40] T. Suzuki, Y. Ishii, A. Itami, K. Ushioda, N. Yoshinaga, H. Tezuka, Influence of Precipitates on Behavior of Recrystallization and Grain Growth in Extra Low Carbon Ti-Bearing Cold-Rolled Steel Sheets, in: H. Yoshinaga, T. Watanabe, N. Takahashi (Eds.), *Grain Growth Polycryst. Mater. II*, Trans Tech Publications, 1996: pp. 673–678. doi:10.4028/www.scientific.net/MSF.204-206.673.
- [41] W. Hume-Rothery, *The Structures of Alloys of Iron: An Elementary Introduction*, reprint, r, Elsevier, Great Britain, 2016.
- [42] L. Wang, S. Parker, A. Rose, G. West, R. Thomson, Effects of Solute Nb Atoms and Nb Precipitates on Isothermal Transformation Kinetics from Austenite to Ferrite, *Metall. Mater. Trans. A.* 47 (2016) 3387–3396. doi:10.1007/s11661-016-3548-x.
- [43] S.D. Cateau, H.P. Van Landeghem, J. Teixeira, J. Dulcy, M. Dehmas, S. Denis, A. Redjaïmia, M. Courteaux, Carbon and nitrogen effects on microstructure and kinetics associated with bainitic transformation in a low-alloyed steel, *J. Alloys Compd.* 658 (2016) 832–838. doi:10.1016/j.jallcom.2015.11.007.
- [44] GATAN, Murano and Microtest In-Situ Stages, (2018).

- <http://www.gatan.com/products/sem-specimen-stages/murano-and-microtest-situ-stages> (accessed March 30, 2018).
- [45] Oxford Instruments, EBSD - Electron Backscatter Diffraction, (2017). <https://www.oxford-instruments.com/products/microanalysis/ebstd> (accessed April 27, 2017).
- [46] S. Clark, V. Janik, A. Rijkenberg, S. Sridhar, Analysis of the extent of interphase precipitation in V-HSLA steels through in-situ characterization of the γ/α transformation, *Mater. Charact.* 115 (2016) 83–89. doi:10.1016/j.matchar.2016.03.021.
- [47] X. Huang, D. Juul Jensen, N. Hansen, Effect of grain orientation on deformation structure and recrystallization behaviour of tensile strained copper, in: S.H.G. Sakai T. (Ed.), 4th Int. Conf. Recryst. Relat. Phenom., Japan Institute of Metals, 1999: pp. 161–166.
- [48] C. Moussa, M. Bernacki, R. Besnard, N. Bozzolo, About quantitative EBSD analysis of deformation and recovery substructures in pure Tantalum, in: IOP Conf. Ser. Mater. Sci. Eng., IOP Publishing, 2015: p. 12038. <http://stacks.iop.org/1757-899X/89/i=1/a=012038>.
- [49] T.B. Britton, High Angular Resolution EBSD (HR-EBSD), (2016) 1–48. <https://drive.google.com/file/d/0BzcVPW0PZrI9X2NvcWtzakVsSTA/view>.
- [50] R. Cornell, H.K.D.H. Bhadeshia, Decarburization of Steel, (2018). <https://www.phase-trans.msm.cam.ac.uk/abstracts/M0.html> (accessed March 30, 2018).
- [51] J. Scott, F.T. Docherty, M. MacKenzie, W. Smith, B. Miller, C.L. Collins, A.J. Craven, Sample preparation for nanoanalytical electron microscopy using the FIB lift-out method and low energy ion milling, in: J. Phys. Conf. Ser., IOP Publishing, 2006: p. 223. <http://stacks.iop.org/1742-6596/26/i=1/a=053>.
- [52] Y.Q. Wang, S.J. Clark, V. Janik, R.K. Heenan, D.A. Venero, K. Yan, D.G. McCartney, S. Sridhar, P.D. Lee, Investigating nano-precipitation in a V-containing HSLA steel using small angle neutron scattering, *Acta Mater.* 145 (2018) 84–96. doi:10.1016/j.actamat.2017.11.032.
- [53] C.A. Schneider, W.S. Rasband, K.W. Eliceiri, NIH Image to ImageJ: 25 years of image analysis, *Nat. Methods.* 9 (2012) 671. doi:10.1038/nmeth.2089.
- [54] A.M. Page, Quantifying Precipitate Size and Distribution in Aluminum Alloy Friction Stir Welds for Aerospace Structures, (2014). [https://uncw.edu/csurf/explorations/documents/volume 9 2014/page.pdf](https://uncw.edu/csurf/explorations/documents/volume%209%202014/page.pdf).
- [55] A. Karmakar, S. Mukherjee, S. Kundu, D. Srivastava, R. Mitra, D. Chakrabarti, Effect of composition and isothermal holding temperature on the precipitation hardening in Vanadium-microalloyed steels, *Mater. Charact.* 132 (2017) 31–40. doi:10.1016/j.matchar.2017.08.003.
- [56] D.I. Kim, K.H. Oh, H.C. Lee, Statistical Analysis on the Development of Recrystallization Texture in IF Steel, in: Textures Mater. - ICOTOM 13, Trans Tech Publications, 2002: pp. 839–844. doi:10.4028/www.scientific.net/MSF.408-412.839.
- [57] H.J. Bunge, Mathematical methods of texture analysis, Akad. Berlin. (1969).
- [58] M. Almojil, Deformation and Recrystallisation in Low Carbon Steels, 2010.
- [59] T. Ogawa, N. Maruyama, N. Sugiura, N. Yoshinaga, Incomplete Recrystallization and Subsequent Microstructural Evolution during Intercritical Annealing in Cold-rolled Low Carbon Steels, *ISIJ Int.* 50 (2010) 469–475. doi:10.2355/isijinternational.50.469.
- [60] H. Réglé, Mechanisms of microstructure and texture evolution during recrystallization of ferritic steels sheets, in: G. Gottstein, D.A. Molodov (Eds.), First Jt. Int. Conf. Recryst. Grain Growth, Springer-Verlag, Berlin, 2001: pp. 707–717.
- [61] C.W. Sinclair, F. Robaut, L. Maniguet, J.D. Mithieux, J.H. Schmitt, Y. Brechet, Recrystallization and Texture in a Ferritic Stainless Steel: an EBSD Study, *Adv. Eng.*

- Mater. 5 (2003) 570–574. doi:10.1002/adem.200300377.
- [62] T. Gladman, On the Theory of the Effect of Precipitate Particles on Grain Growth in Metals, Proc. R. Soc. London. Ser. A. Math. Phys. Sci. 294 (1966) 298–309. doi:10.1098/rspa.1966.0208.
- [63] N. Prasad, S. Kumar, P. Kumar, S.N. Ojha, Mechanical properties of a cold-rolled annealed HSLA steel, J. Mater. Sci. 26 (1991) 5158–5162. doi:10.1007/BF01143207.
- [64] D. Raabe, K. Lücke, Rolling and Annealing Textures of BCC Metals, in: Textures Mater. - ICOTOM 10, Trans Tech Publications, 1994: pp. 597–610. doi:10.4028/www.scientific.net/MSF.157-162.597.
- [65] M. Hölscher, D. Raabe, K. Lucke, Rolling and recrystallization textures of bcc steels, Steel Res. 62 (1991).
- [66] W.W. Mullins, The effect of thermal grooving on grain boundary motion, Acta Metall. 6 (1958) 414–427.
- [67] I. Samajdar, B. Verlinden, P. Van Houtte, D. Vanderschueren, Recrystallisation kinetics in IF-steel: A study on the sluggish recrystallisation behaviour, Scr. Mater. 37 (1997) 869–874. doi:10.1016/S1359-6462(97)00185-1.
- [68] I. Samajdar, B. Verlinden, P.V. Houtte, D. Vanderschueren, γ -Fibre recrystallization texture in IF-steel: an investigation on the recrystallization mechanisms, Mater. Sci. Eng. A. 238 (1997) 343–350. doi:10.1016/S0921-5093(97)00455-3.
- [69] M.Z. Quadir, B.J. Duggan, Deformation banding and recrystallization of α fibre components in heavily rolled IF steel, Acta Mater. 52 (2004) 4011–4021.
- [70] W.B. Hutchinson, Deformation substructures and recrystallisation, in: Mater. Sci. Forum, Trans Tech Publ, 2007: pp. 13–22.
- [71] J. Pak, D.W. Suh, H. Bhadeshia, Displacive phase transformation and surface effects associated with confocal laser scanning microscopy, Metall. Mater. Trans. A. 43 (2012) 4520–4524.
- [72] M.M. Nowell, D.P. Field, S.I. Wright, T.M. Lillo, In-Situ EBSD Investigation of Recrystallization in ECAE Processed Copper, in: Recryst. Grain Growth, Trans Tech Publications, 2004: pp. 1401–1406. doi:10.4028/www.scientific.net/MSF.467-470.1401.
- [73] Y. Jin, B. Lin, M. Bernacki, G.S. Rohrer, A.D. Rollett, N. Bozzolo, Annealing twin development during recrystallization and grain growth in pure nickel, Mater. Sci. Eng. A. 597 (2014) 295–303. doi:https://doi.org/10.1016/j.msea.2014.01.018.
- [74] C.S. Barrett, L.H. Levenson, Analysis of the cold rolling texture of iron, Trans. Amer. Inst. Min. Metall. Eng. 145 (1941) 281.
- [75] H. Inagaki, Fundamental Aspect of Texture Formation in Low Carbon Steel, ISIJ Int. 34 (1994) 313–321. doi:10.2355/isijinternational.34.313.
- [76] J. Grewen, G. Wassermann, Textures in research and practice, Springer, 1969.
- [77] N. Rajmohan, Y. Hayakawa, J.A. Szpunar, J.H. Root, The determination of orientation-dependent stored energy using neutron diffraction, Phys. B Condens. Matter. 241–243 (1997) 1225–1227. doi:https://doi.org/10.1016/S0921-4526(97)00834-X.